J. Fluid Mech. (2023), *vol*. 961, A15, doi:10.1017/jfm.2023.213

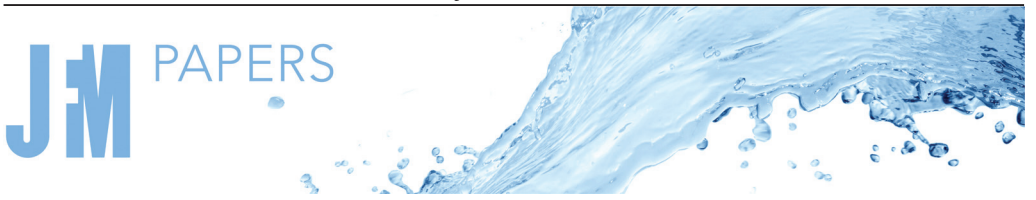

Effect of surfactants during drop formation in a microfluidic channel: a combined experimental and computational fluid dynamics approach

M. Kalli[1], P. Pico[2], L. Chagot[1], L. Kahouadji[2], S. Shin[3], J. Chergui[4], D. Juric[4,5], O.K. Matar[2,†] and P. Angeli[1,†]

[1]Chemical Engineering Department, University College London, Torrington Place, London WC1E 7JE, UK

[2]Department of Chemical Engineering, Imperial College London, South Kensington Campus, London SW7 2AZ, UK

[3]Department of Mechanical and System Design Engineering, Hongik University, Seoul 04066, Republic of Korea

[4]Centre National de la Recherche Scientifique (CNRS), Laboratoire Interdisciplinaire des Sciences du Numérique (LISN), Université Paris Saclay, 91400 Orsay, France

[5]Department of Applied Mathematics and Theoretical Physics, University of Cambridge, Cambridge CB3 0WA, UK

(Received 20 July 2022; revised 23 February 2023; accepted 6 March 2023)

The effect of surfactants on the flow characteristics during rapid drop formation in a microchannel is investigated using high-speed imaging, micro-particle image velocimetry and numerical simulations; the latter are performed using a three- dimensional multiphase solver that accounts for the transport of soluble surfactants in the bulk and at the interface. Drops are generated in a flow-focusing microchannel, using silicone oil (4.6 mPa s) as the continuous phase and a 52 % w/w glycerol solution as the dispersed phase. A non-ionic surfactant (Triton X-100) is dissolved in the dispersed phase at concentrations below and above the critical micelle concentration. Good agreement is found between experimental and numerical data for the drop size, drop formation time and circulation patterns. The results reveal strong circulation patterns in the forming drop in the absence of surfactants, whose intensity decreases with increasing surfactant concentration. The surfactant concentration profiles in the bulk and at the interface are shown for all stages of drop formation. The surfactant interfacial concentration is large at the front and the back of the forming drop, while the neck region is almost surfactant free. Marangoni

† Email addresses for correspondence: o.matar@imperial.ac.uk, p.angeli@ucl.ac.uk

stresses develop away from the neck, contributing to changes in the velocity profile inside the drop.

Key words: drops, microfluidics, multiphase flow

1. Introduction

Microfluidic channels are widely used to produce droplets with controlled size and low polydispersity index, which are important in applications such as emulsification, inkjet printing, cosmetics and healthcare (Lawrence & Rees 2000; Yang *et al.* 2018; Park, Kim & Kim 2021). Surfactants are commonly added during drop formation to modify the interfacial properties and improve the stability of the emulsions. The presence of surfactant molecules significantly affects the nonlinear drop formation process and thus the final size (Chen, Xu & Luo 2015). In the common dripping regime, drop formation depends on the balance between the interfacial tension and the drag forces, with the latter being the combination of shear and pressure forces (Xu *et al.* 2006). As a result, a lower interfacial tension caused by surfactant addition will result in smaller and more rapidly forming drops. As seen in previous work, the small characteristic time scales that are present in microfluidics can lead to interfacial tension values different from the equilibrium ones, which are often used in the calculation of capillary numbers Ca (Kalli & Angeli 2022) and in predictive equations for drop size. Additionally, shear stresses from high continuous phase velocities can redistribute surfactant molecules at the interface, which will cause interfacial tension gradients and thus Marangoni stresses (Kovalchuk & Simmons 2021). For surfactants that result in a large decrease in interfacial tension, the effect of interface retardation at low surfactant concentrations can be sufficiently large to change the velocity fields close to the interface and inside the drop, due to Marangoni stresses in the opposite direction to the flow. At high concentrations, surfactant exchange between the bulk and the interface is fast and interface remobilisation is seen at high velocities (Martin & Hudson 2009). Since both observations will greatly impact the final surfactant transport, it is important to study the behaviour of such surfactants at different concentrations, below and above the critical micelle concentration (CMC).

As first reported by Garstecki, Stone & Whitesides (2005), drop formation in the dripping regime is typically divided into three stages called expansion, necking and pinch-off. Following drop detachment, the interface pulls towards the inlet before recoiling in the downstream direction. At this stage, drop growth is mainly in the streamwise direction forming a parabolic interface profile and is dominated by interfacial tension. Once the pressure builds up due to restriction of the inlet from the forming drop, the drag force overcomes the interfacial tension force and a reversal of the interface curvature is observed, which indicates the beginning of the necking stage. The neck width decreases until the drag force is large enough to cause drop detachment and thus pinch-off. In recent studies (Wang *et al.* 2009; Xu *et al.* 2012), it was found that high dispersed phase flow rates enhance convection and surfactant mass transfer from the continuous phase to the interface, which explain the reduced interfacial tension values at short formation times. Furthermore, it was found that absorption and mass transfer rates can compete with drop formation times (Kalli, Chagot & Angeli 2022). Investigating the transport of surfactants during each phase of the drop formation process is vital in understanding the impact on the final drop size.

Improvements in experimental techniques allow the accurate visualisation of flows inside microchannels, which can be used to explore the effects of surfactant transport.

Kiratzis *et al.* (2022) used ghost particle velocimetry to study the effect of surfactant concentration, continuous phase velocity and viscosity on drop formation in rectangular channels. Results revealed smaller velocities at the interface when a surfactant of the same family but with a slower adsorption rate (lower CMC) was present, suggesting the presence of Marangoni stresses. In addition, larger internal circulation inside the drops was seen at higher continuous phase viscosity during the expansion stage. Roumpea *et al.* (2019) used an innovative two-colour micro-particle image velocimetry (μPIV) technique to study velocity fields in a flow-focusing microchannel in the presence of two cationic surfactants of the same family but different adsorption kinetics (C_{12}TAB, dodecyltrimethylammonium bromide and C_{16}TAB, hexadecyltrimethylammonium bromide). Addition of surfactant in the dispersed phase resulted in higher velocities at the tip and more uniform velocity fields inside the drop, which was attributed to surfactant accumulation at the tip that increases the interface rigidity in that area. A second observation was the decrease in the circulation inside the drop, which was again attributed to Marangoni effects that caused the interface to move in the opposite direction to the flow and opposed circulation. Similar effects were seen when a non-ionic surfactant (Span80) was added in the continuous oil phase, in a T-junction channel (Riaud *et al.* 2018). A stagnant cap was observed in this case near the drop tip that split the forming drop interface into a mobile and a rigid region. The resulting Marangoni force in the opposite direction of the forming drop resisted the flow circulation. Studies on drop formation in a flow-focusing microchannel by Carrier *et al.* (2015) revealed a flow inversion during pinch-off and weaker recirculation at the base of the drop compared with its front, upon addition of SDS (sodium dodecylsulphate) surfactant. Changes in circulation within surfactant-laden drops using μPIV were investigated in emulsions produced in a tapered microchannel leading to a geometrical constriction (Leong, Gai & Tang 2018). It was found that vortical structures forming when the drops passed the constriction, increase circulation up to 2.5 times compared with droplet mixing at the channel constriction.

Despite the work reviewed above, there are still important limitations to be addressed in order to fully understand the effect of surfactant on the drop formation process. As previously mentioned, it is essential to know the surfactant distribution at the interface as it can accumulate at the tip and cause Marangoni flows as the drop forms. The surfactant concentration at the interface is very challenging to obtain experimentally (Dussaud, Matar & Troian 2005), especially during flow. Even if a fluorescent surfactant is used, the powerful intensity of the laser needed for visualisation can cause photobleaching (Eggeling *et al.* 1998), which is non-reversible. Another issue is self-quenching (Aicolina, Leaver & Stapleton 1989; Li *et al.* 2022), where the total emitted intensity can change upon temperature, pressure or pH fluctuations. Additionally, most fluorescent surfactants are soluble in solvents such as chloroform and dimethylformamide, which can be toxic. Since most fluorescently tagged surfactants are synthesised by adding a fluorescent group to the amphiphilic structure of the surfactant, they usually result in heavier molecules that exhibit low interfacial activity (i.e. small reduction in interfacial tension with concentration) or slow adsorption kinetics, especially when compared with the fast drop formation process. Dong, Weheliye & Angeli (2019) used planar laser induced fluorescence to capture the spatio-temporal distribution of a fluorescent surfactant during the coalescence of a mm size drop with a flat surface, using a laser sheet with 1 mm thickness. This dimension is an order of magnitude larger than typical microchannel length scales. On the other hand, the volume illumination used for microchannel laser induced fluorescence studies is not ideal when tracing molecules at a three-dimensional interface.

The complex phenomena of drop formation in microchannels have also been investigated through numerical approaches. Computational fluid dynamics (CFD) simulations in particular are a powerful tool to overcome most of the above-mentioned experimental limitations and extract useful information related to the dynamics of the flow. Numerous CFD investigations based on volume-of-fluid and level-set methods have been conducted to determine the role of operating conditions on the drop formation process in surfactant-free systems. These studies have revealed the interplay between capillarity, inertia and viscosity for different microfluidic junction geometries and their effects on drop formation (Van der Graaf *et al.* 2006; Li *et al.* 2012; Lan *et al.* 2014; Ngo *et al.* 2015; Zhao *et al.* 2015; Soh, Yeoh & Timchenko 2016; Kahouadji *et al.* 2018; Filimonov, Wu & Sundén 2021). Recent studies in the presence of surfactants have provided a detailed description of the heterogeneous distribution of surfactant concentration at the interface and the effect on drop formation time and drop size. Riaud *et al.* (2018) performed numerical simulations inside a T-junction microchannel for a Span80-octane/water mixture and compared the results against μPIV experiments. The authors found that the interfacial distribution of surfactants on growing droplets is not uniform but surfactants tend to concentrate at the droplet tip. They also reported that surfactant adsorption is faster than drop formation at low velocities and low Ca. As Ca is increased, either by lowering the interfacial tension or by increasing the inlet velocity, the characteristic drop formation time is reduced and thus adsorption becomes slower than formation time. The authors showed that droplet volume increases with increasing dispersed phase flow rate and decreasing Ca; both parameters are therefore necessary to predict the drop size. Jin, Gupta & Stebe (2006) studied the effect of soluble surfactants on drop necking and used a nonlinear model to relate interfacial tension to surfactant concentration at the interface, by accounting for maximum surfactant packing at the interface. The analysis revealed that a family of necks formed, as a result of a primary and a secondary thinning rate of the neck, depending on the local accumulation of surfactants, and demonstrated that drop detachment behaviour can be used to quantify surfactant dynamics. Antonopoulou *et al.* (2021) performed experimental and numerical studies on the flow behaviour during inkjet printing and explained the effect different surfactants have on pinch-off during jetting.

This paper combines unique experimental and numerical approaches to investigate surfactant transport in the bulk, distribution at the interface and Marangoni phenomena during the fast drop formation process in a microfluidic channel. A non-ionic ($\mathrm{CMC}_{TX100} = 3.5$ mM) surfactant is used in the dispersed aqueous phase at concentrations below and above the CMC. A novel high-speed μPIV system is able to follow all stages of the fast drop formation process, which is a key improvement compared with previous works (Riaud *et al.* 2018; Roumpea *et al.* 2019). The CFD simulations include the exchange of surfactant between the bulk of the drop and the interface, as opposed to previous works that considered only transport at the interface (Riaud *et al.* 2018; Antonopoulou *et al.* 2021). The effect of surfactant on the vortical structures and velocity fields are discussed for the different stages of drop formation. The CFD simulations provide information on surfactant concentrations at the interface that cannot be obtained experimentally. In addition, they reveal the vortical structures very close to the interface where measurements are not accurate because of the low concentration of the PIV tracer particles in this region (i.e. at the neck region just before pinch-off). They also enable investigations of the drop in three dimensions, which are very challenging to obtain experimentally. The experiments on the other hand provide data on the effect of the surfactant at high concentrations above the CMC, which is beyond the capabilities of the current model. The Marangoni stresses at the interface are calculated and presented as a function of time, space, and dispersed phase flow rate for the first time during the whole drop formation process.

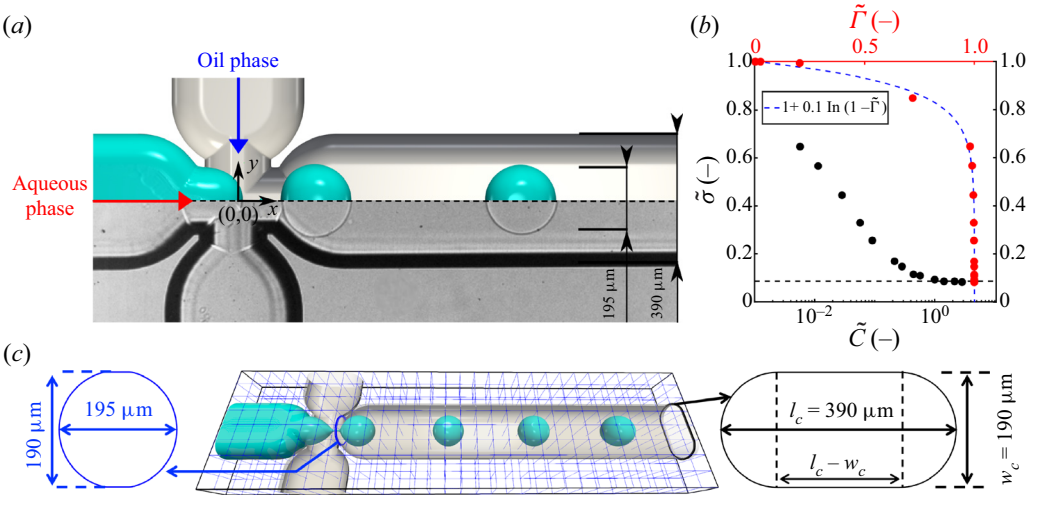

Figure 1. (*a*) Numerical configuration, and an illustrative snapshot of a top view of the interface (top), and the corresponding high-speed image from experiments (bottom); (*b*) interfacial tension isotherm for TX100 surfactant showing the variation of equilibrium interfacial tension, σ. Black points represent dimensionless $\tilde{\sigma}$ (normalised by the surfactant-free value of interfacial tension, σ_s) with the semi-log variation of the dimensionless surfactant bulk concentration $\tilde{C}$ (normalised by the CMC). Red points represent the dimensionless interfacial surfactant concentration, $\tilde{\Gamma}$ (normalised by Γ saturation value, Γ_∞) obtained using (3.7) and $\Gamma = \Gamma_\infty K_L C/(1 + K_L C)$. The blue dashed line represents the fitting of $\tilde{\sigma} = 1 + 0.1\ln(1 - \tilde{\Gamma})$; (*c*) geometrical details of the microfluidic channel decomposed into $240 = 30 \times 8 \times 1$ subdomains. Each subdomain contains an equal and structured mesh resolution of 32^3, for a total of $960 \times 256 \times 32$ cells.

2. Experimental methods

2.1. *Droplet generation*

The experiments were performed in a glass flow-focusing microchannel from Dolomite Microfluidics (Part No. 3000436) already used in previous works (Kovalchuk *et al.* 2018; Roumpea *et al.* 2019). At the cross-junction the inlet dimensions are 195 µm × 190 µm (width × depth) and the dimensions of the main channel are 390 µm × 190 µm (width × depth). The continuous phase was introduced via the side channels and then the aqueous phase via the central channel of the junction (see figure 1*a*). For all configurations, silicone oil (Clearco, density: $\rho_c = 920\,\mathrm{kg\,m^{-3}}$, viscosity: $\mu_c = 4.6\,\mathrm{mPa\,s}$ at 20 °C) was used as the continuous phase and a mixture of 52 % w/w glycerol and 48 % w/w water (Sigma Aldrich, ≥99.5 %, density: $\rho_d = 1132\,\mathrm{kg\,m^{-3}}$, viscosity $\mu_d = 6.8\,\mathrm{mPa\,s}$ at 20 °C) with and without surfactant was selected as the dispersed phase. Based on the work of Kalli *et al.* (2022), the flow rates were selected to form drops in the dripping regime. Using syringe pumps (KDS Scientific, $\pm 5 \times 10^{-9}\,\mathrm{ml\,min^{-1}}$), the continuous phase was introduced with a total flow rate $Q_c = 0.12\,\mathrm{ml\,min^{-1}}$, while the dispersed phase had a flow rate of $Q_d = 0.01, 0.02\,\mathrm{ml\,min^{-1}}$. To observe the impact of interfacial tension on the drop formation, several concentrations of the non-ionic surfactant Triton X-100 (TX100), (Acros organics, $M_w = 646.85\,\mathrm{g\,mol^{-1}}$, ≥95 %) were dissolved in the dispersed phase at concentrations of (0.1, 0.2, 0.6, 1.0, 1.4, 2.1, 2.9, 4.3, 5.7, 8.6) × CMC. Figure 1(*b*) shows the equilibrium interfacial tension values (σ), normalised by the final equilibrium interfacial tension value at CMC = 3.5 mM ($\sigma_{\Gamma=\Gamma_\infty} = 2.9\,\mathrm{mN\,m^{-1}}$) as measured using a Du Noüy ring attached to a Force K100 Tensiometer (Krüss GmbH).

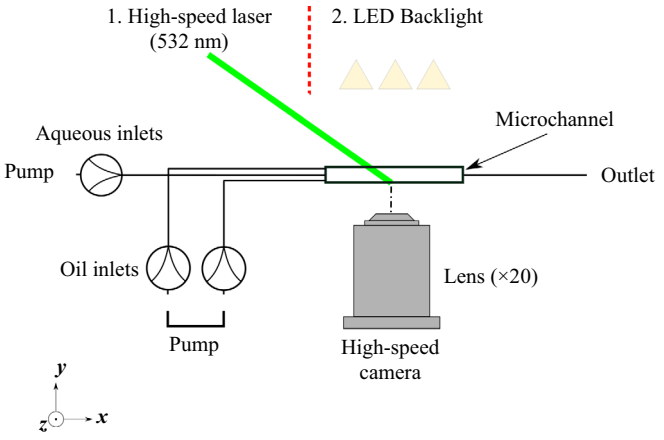

Figure 2. Experimental set-up of the HSI and μPIV techniques.

2.2. *Optical techniques*

The experimental set-up is shown in figure 2. Two different illumination modes were used for the μPIV or the high-speed imaging (HSI). To allow full optical access for all measurements and avoid optical distortions, in particular close to the channel wall, both phases were selected to match the refractive index of the glass microchannel ($n_i = 1.39$). For both modes, the images were taken with a 12-bit high-speed camera (Phantom v1212, 1280 $\times$ 800 pixels resolution). In the HSI experiments, the acquisition frequency was 10 000 Hz and the camera was equipped with a Nivatar $\times$20 zoom lens and an LED backlight for illumination. Results were averaged for at least 15 drops (drop size polydispersity $\leq$1.2 %). The experimental error is 3 µm per pixel for the spatial resolution and 0.1 ms for the time resolution.

The high-speed μPIV experiments were performed by switching modes from the LED light (2) to the laser source (1) as shown in figure 2. The laser illumination was generated with a high-speed 60 W pulsed Nd-Yag (Litron), which allows the observation in time of the droplet generation. The dispersed phase was seeded with 1 µm carboxylate-modified microspheres FluoSpheres, with an absorbance of 542 nm and an emission of 612 nm. For the PIV image pairs, the camera was equipped with a $\times$20 microscope lens (Mitutoyo Ltd) and focal depth of 1.6 µm. The lens was mounted with a high-pass filter (>565 nm) to eliminate reflections from the channel walls. Moreover, to be able to follow the interface during the PIV measurements, a small amount of rhodamine B (with absorbance of 510 nm and emission of 610 nm) was added in the dispersed phase (0.05 ppm). The high-speed μPIV allows measurements in the channel centre during drop formation, which follow the whole process from the expansion $t = t_{exp}$ to the pinch-off stage $t = t_{pin}$. For each measurement, 2000 image pairs were acquired at a frequency of 3000 Hz which represent $\sim$20 drop formation cycles. The measurements were performed in the entire channel width ($y/l_c \in [-1, 1]$, with y the transverse direction) and around the droplet emergence area ($x/l_c \in [-2, 2]$, with x the streamwise direction). The local coordinate system is defined in figure 1(a) where $(x, y) = (0, 0)$ is the centre of the cross-junction. All velocity fields were computed with the free PIV software CPIV-IMFT developed at IMFT. It is based on an FFT cross-correlation method with peak-locking reduction schemes and parallelisation. In the processing, 16 $\times$ 16 pixels interrogation boxes and 50 % overlap were used, yielding a grid resolution of 1.4 µm.

3. Numerical formulation, scaling and validation

3.1. *Numerical formulation and problem statement*

As mentioned in § 2, the microfluidic channel used in this study consists of a combination of both cross-junction and flow-focusing devices. Its computational representation and dimensions are illustrated in figure 1(*c*). The four branches of this device are identical with an oval cross-section shape of length $l_c = 390\,\mu\text{m}$ and width $w_c = 190\,\mu\text{m}$. This cross-section is comprised a rectangular piece of dimensions $w_c \times (l_c - w_c)$ connected to two semicircles of diameter w_c. Figure 1(*c*) also shows the three-dimensional computational domain and its decomposition into $240 = 30 \times 8 \times 1$ sub-domains used for the message passing interface computing protocol. The numerical construction of this device follows a similar approach as that used in Kahouadji *et al.* (2018). This approach bypasses the typical obstacles in construction and meshing that arise when handling complex geometries by employing a static distance function for several primitive objects (e.g. cylinders, planes, and tori), and simple algebraic operations between them, such as 'union' and 'intersection'.

The flow is considered incompressible and both the continuous and dispersed phases are assumed to be Newtonian. The following scaling is adopted to non-dimensionalise the equations governing the flow dynamics coupled to the surfactant transport in the bulk of the dispersed phase and at the interface:

$$\left.\begin{gathered}\tilde{\boldsymbol{x}} = \frac{\boldsymbol{x}}{l_c}, \quad \tilde{\boldsymbol{u}} = \frac{\boldsymbol{u}}{U_{sc}}, \quad \tilde{t} = \frac{t}{l_c/U_{sc}}, \quad \tilde{p} = \frac{p}{\mu_c U_{sc}/l_c}, \quad \tilde{\sigma} = \frac{\sigma}{\sigma_s}, \\ \tilde{\Gamma} = \frac{\Gamma}{\Gamma_\infty}, \quad \tilde{C} = \frac{C}{CMC}, \quad \widetilde{C_s} = \frac{C_s}{CMC}.\end{gathered}\right\} \tag{3.1}$$

Here, the tildes designate dimensionless quantities, and $\boldsymbol{x}$, t, $\boldsymbol{u}$ and p are the spatial coordinate, time, velocity and pressure, respectively; the interface surfactant concentration is represented by Γ, C and C_s are the concentrations at the bulk and the bulk sub-phase, located immediately adjacent to the interface, respectively (Shin *et al.* 2018; Batchvarov *et al.* 2020; Constante-Amores *et al.* 2020, 2021*a*,*b*), and σ is the local interfacial tension varying as function of Γ. The length scale l_c, the average surface velocity of the continuous phase in the main portion of the channel, $U_{sc} = Q_c/A$ $(A = l_c w_c + (\pi/4 - 1)w_c^2)$, the interfacial tension in a surfactant-free system, σ_s, the saturation interfacial concentration, Γ_∞, and the CMC, are used as the characteristic length, velocity, interfacial tension and interfacial and bulk surfactant concentration scales, respectively; ρ_c and μ_c are the continuous phase density and dynamical viscosity, respectively. The dimensionless governing equations for the flow and surfactant transport are formulated in (3.2)–(3.7):

$$\nabla \cdot \tilde{\boldsymbol{u}} = 0, \quad \tilde{\rho} Re \left(\frac{\partial \tilde{\boldsymbol{u}}}{\partial \tilde{t}} + \tilde{\boldsymbol{u}} \cdot \nabla \tilde{\boldsymbol{u}} \right) = -\nabla \tilde{p} + \nabla \cdot \left[\tilde{\mu} (\nabla \tilde{\boldsymbol{u}} + \nabla \tilde{\boldsymbol{u}}^{\mathrm{T}}) \right] + \frac{1}{Ca} \int_{\tilde{A}} (\tilde{\sigma} \tilde{\kappa} \boldsymbol{n} + \nabla_s \tilde{\sigma})\, \delta \left(\tilde{\boldsymbol{x}} - \tilde{\boldsymbol{x}}_f \right) \mathrm{d}\tilde{A}, \tag{3.2}$$

$$\left.\begin{aligned}\tilde{\rho}\,(\boldsymbol{x}, t) &= \frac{\rho_d}{\rho_c} + \left(1 - \frac{\rho_d}{\rho_c}\right) \mathcal{H}\,(\boldsymbol{x}, t)\,, \\ \tilde{\mu}\,(\boldsymbol{x}, t) &= \frac{\mu_d}{\mu_c} + \left(1 - \frac{\mu_c}{\mu_d}\right) \mathcal{H}\,(\boldsymbol{x}, t)\,,\end{aligned}\right\} \tag{3.3}$$

$$\frac{\partial \tilde{\Gamma}}{\partial \tilde{t}} + \nabla_s \cdot (\tilde{\Gamma}\tilde{\boldsymbol{u}}_t) = \frac{1}{Pe_s}\nabla_s^2 \tilde{\Gamma} + Bi\left(k\widetilde{C}_s(1-\tilde{\Gamma}) - \tilde{\Gamma}\right), \tag{3.4}$$

$$\frac{\partial \tilde{C}}{\partial \tilde{t}} + \tilde{\boldsymbol{u}} \cdot \nabla \tilde{C} = \frac{1}{Pe_c}\nabla \cdot (\nabla \tilde{C}), \tag{3.5}$$

$$\boldsymbol{n} \cdot \nabla \tilde{C}|_{interface} = -Pe_c DaBi\left(k\widetilde{C}_s(1-\tilde{\Gamma}) - \tilde{\Gamma}\right), \tag{3.6}$$

$$\tilde{\sigma} = \max\left(\epsilon_\sigma, 1 + \beta_s \ln\left(1-\tilde{\Gamma}\right)\right), \tag{3.7}$$

with ϵ_σ set to 0.05, a numerical threshold to avoid non-physical negative values for $\tilde{\sigma}$. The dimensionless numbers shown in the above equations are defined by

$$\left.\begin{gathered} Re = \frac{\rho_c U_{sc} l_c}{\mu_c}; \quad Ca = \frac{\mu_c U_{sc}}{\sigma_s}; \quad Pe_c = \frac{U_{sc} l_c}{D_c}; \quad Pe_s = \frac{U_{sc} l_c}{D_s}; \quad Bi = \frac{k_d l_c}{U_{sc}}; \\ Da = \frac{\Gamma_\infty}{l_c CMC}; \quad k = \frac{k_a CMC}{k_d}, \end{gathered}\right\} \tag{3.8}$$

where Ca and Re are the liquid capillary and Reynolds numbers, respectively; in which μ_c is the continuous phase viscosity; Pe_c and Pe_s are the bulk and interfacial Péclet numbers that represent the interplay between convective and diffusive forces for the surfactant species at the bulk and interface, respectively, in which D_c and D_s are the (constant) surfactant diffusion coefficients in the bulk continuous phase and the plane of the interface, respectively. The Biot number, Bi, represents the competition between the time scales of desorption and convection, characterised by k_d^{-1} and l_c/U_{sc}, respectively. Finally, k represents the competition between adsorption and desorption time scales, characterised by $(k_a CMC)^{-1}$ and k_d^{-1}, respectively. Lastly, the Damköhler number, Da, provides a dimensionless measure of interfacial saturation with surfactant.

The continuity and momentum equations (3.2) are written in a three-dimensional Cartesian domain using a single-fluid formulation. $\mathcal{H}(\tilde{\boldsymbol{x}}, \tilde{t})$ represents a smoothed Heaviside function that takes the value of zero in the continuous phase and unity in the dispersed phase. The normal and tangential components of the interfacial tension force are expressed by the last two terms on the right-hand side of (3.2), respectively. The latter term representing the interfacial tension gradients across the interface, which give rise to Marangoni stresses; $\tilde{\kappa}$ corresponds to the interface curvature and $\delta(\tilde{\boldsymbol{x}} - \tilde{\boldsymbol{x}}_f)$ is the three-dimensional Dirac delta function equal to unity at the interface ($\tilde{\boldsymbol{x}} = \tilde{\boldsymbol{x}}_f$) and zero elsewhere. In (3.4), $\nabla_s = (\boldsymbol{I} - \boldsymbol{nn}) \cdot \nabla$ is the surface gradient operator, $\boldsymbol{n}$ is the outward-pointing unit normal to the interface, and $\boldsymbol{I}$ is the identity tensor; $\tilde{\boldsymbol{u}}_t = (\tilde{\boldsymbol{u}}_s \cdot \tilde{\boldsymbol{t}})\tilde{\boldsymbol{t}}$ corresponds to the tangential velocity, where $\tilde{\boldsymbol{u}}_s$ is the surface velocity, and $\boldsymbol{t}$ is the unit vector tangent to the interface. The last terms on the right-hand side of (3.4) and (3.7) represent the source term for surfactant exchange between the interface and the section of the bulk immediately adjacent to the interface.

As seen from figure 1(*b*) and (3.7), the dependence of σ on Γ is described by a nonlinear Langmuir equation of state in which $\beta_s = \Re T \Gamma_\infty / \sigma_s$ modulates this dependency, as suggested by Muradoglu & Tryggvason (2014); $\Re$ and T are the ideal gas constant and the temperature, respectively. The components of the interfacial tension force that induce Marangoni stresses can be written in terms of Γ by

$$\frac{1}{Ca}\nabla_s \tilde{\sigma} \cdot \boldsymbol{t} \equiv \frac{\tilde{\tau}}{Ca} = -Ma \frac{1}{(1-\tilde{\Gamma})} \nabla_s \tilde{\Gamma} \cdot \boldsymbol{t}, \tag{3.9}$$

Physical properties	TX100
Γ_∞ (mol m^{-2})	1.42×10^{-6}
K_L (m^3 mol^{-1})	1585.00
k_d (s^{-1})	0.0065
k_a (m^3 mol^{-1} s^{-1})	10.3
$\mathcal{D}$ (m^2 s^{-1})	5×10^{-11}

Table 1. Physical properties of TX100 surfactant*.
*k_d was obtained from Gassin *et al.* (2012) and the rest of the parameters were calculated experimentally as explained in § 3.1

where $\tilde{\tau}$ is the dimensionless Marangoni stress and $Ma \equiv \beta_s/Ca$ represents a Marangoni parameter.

From the properties of TX100 and the operating conditions of the system, the relevant dimensionless numbers that characterise the system are given by $Re = 2.35$, $Ca = 4.33 \times 10^{-3}$, $Pe_c = Pe_d = 2.35 \times 10^5$, $Bi = 8.41 \times 10^{-5}$, $Da = 1.04 \times 10^{-3}$, $k = 5.55 \times 10^3$, $\beta_s = 0.10$ and $Ma = 23.08$. We define a capillary time scale as $\tau_{cap} = \sqrt{\rho_c l_c^3/\sigma_s} = 1.31 \times 10^{-3}$ s, a velocity time scale as $\tau_{vel} = \sqrt{\sigma_s/(\rho_c l_c)} = 2.99 \times 10^{-1}$ s and a Marangoni time scale as $\tau_{mar} = \mu_c l_c/\Delta\sigma = 6.16 \times 10^{-5}$ s. Here, it has been assumed that $D_c = D_s = \mathcal{D}$, and Γ_∞ and $K_L = k/CMC$ were found by fitting the experimental data in figure 1(*b*) to the Langmuir–Szyszkowski equation (Teipel & Aksel 2001), as in previous work (Kalli *et al.* 2022); Γ was calculated using the Langmuir equation of state with the measured experimental values of σ for each C (see (3.7) and $\Gamma = \Gamma_\infty K_L C/(1 + K_L C)$) and plotted in a dimensionless form on the secondary axis of figure 1(*b*). Using the literature value of TX100 desorption in water (k_d) (Gassin *et al.* 2012), k_a was calculated using $k_a = K_L k_d$ and shown in table 1. Finally, the diffusion coefficient, $\mathcal{D}$, was estimated using the Wilke–Chang correlation (Wilke & Chang 1955).

Fully three-dimensional direct numerical simulations were performed within the context of the level contour reconstruction method for the interface advection, as previously detailed in Shin & Juric (2002) and Shin *et al.* (2005, 2018) and Shin, Chergui & Juric (2017). This method handles the interface and the forces arising from surface tension through a hybrid front-tracking/level-set technique in conjunction with surfactant transport at the interface and bulk. At the inlet branches, an analytical solution following a Poiseuille profile is set for the velocity, together with a Neumann condition for the pressure ($\partial p/\partial \boldsymbol{n} = 0$). The full derivation of this velocity profile ((3.10) in dimensionless form) in the cross-section shown in figure 1(*c*) (right) can be found in § A. At the outlet, a Neumann condition is specified for both velocity and pressure. The walls are treated as no-slip boundaries. For the surfactant-laden cases, Neumann conditions are set for surfactant concentration on all boundaries, with the exception of the disperse phase inlet. For this inlet, C is specified as a constant value according to the experimental set-up ($\tilde{C} = 0.006$, $\tilde{C} = 0.06$ and $\tilde{C} = 0.21$) and Γ as calculated in figure 1(*b*)

$$\tilde{\boldsymbol{u}}(\tilde{x}, \tilde{y}) = \begin{cases} \tilde{\mathcal{A}}\left(\dfrac{(\tilde{y} - \widetilde{y_0})^2}{\widetilde{R^2}} - 1\right) & \text{if } |\tilde{x} - \widetilde{x_0}| \le \tilde{L} \\ \tilde{\mathcal{A}}\left(\dfrac{(\tilde{x} - \widetilde{x_0} - \tilde{L})^2}{\widetilde{R^2}} + \dfrac{(\tilde{y} - \widetilde{y_0})^2}{\widetilde{R^2}} - 1\right) & \text{otherwise,} \end{cases} \tag{3.10}$$

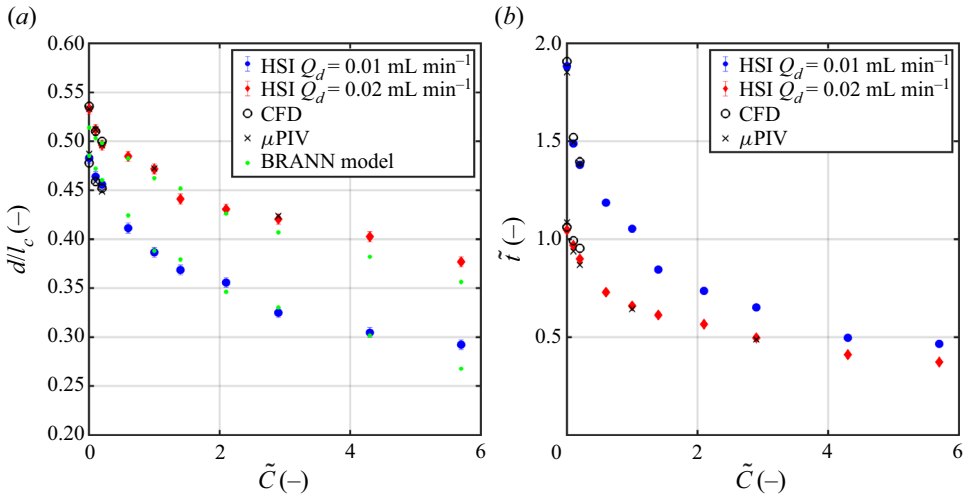

Figure 3. Effect of TX100 concentration on dimensionless drop (*a*) diameter (d/l_c) and (*b*) formation time ($\tilde{t}$) using HSI, μPIV, CFD and the Bayesian regularised artificial neural network (BRANN) model from Chagot *et al.* (2022).

where $\mathcal{A} = -Q/(\frac{8}{3}RL + (\pi/2)R^2)$, Q represents the flow rate of the phase on each inlet (continuous for the two lateral branches and disperse for the central branch), x_0 and y_0 are the coordinates of the centre points of the inlet cross sections, and $R = w_c/2$ and $L = (l_c - w_c)/2$, as highlighted in figure 1(*c*). Each variable has been non-dimensionalised according to the scaling parameters described previously, with $\tilde{\mathcal{A}} = -\tilde{Q}U_{sc}/(\frac{8}{3}\tilde{R}\tilde{L} + (\pi/2)\tilde{R}^2)$.

3.2. *Validation*

The numerical simulation in an identical geometry was validated experimentally with a surfactant-free system in previous work (Kahouadji *et al.* 2018). Further validation with experimental results for surfactant-laden cases is made in this section. As seen in previous work (Kalli *et al.* 2022), a semi-empirical model can be developed to relate the dimensionless drop diameter to the capillary number (and thus the global value of interfacial tension); drop size is found to be proportional to the *Ca* in a microfluidic system in the presence of surfactants. As a result, the addition of surfactant is expected to result in smaller drops with shorter formation times, due to the lower interfacial tension.

Figure 3(*a*) shows the effect of surfactant addition on the drop diameter for $Q_c = 0.12$ and $0.01\,\mathrm{ml\,min^{-1}} \leq Q_d \leq 0.02\,\mathrm{ml\,min^{-1}}$, using HSI, μPIV and CFD. As $\tilde{C}$ increases from 0 to 5.7, the dimensionless drop diameter d/l_c decreases for both flow rates, due to the lower interfacial tension. Larger drops are observed at higher Q_d as expected. The effect of surfactant addition on the drop formation time for $Q_c = 0.12$ and $0.01\,\mathrm{ml\,min^{-1}} \leq Q_d \leq 0.02\,\mathrm{ml\,min^{-1}}$ is shown in figure 3(*b*). As $\tilde{C}$ increases from 0 to 5.7, the dimensionless formation time $\tilde{t}$ decreases for both flow rates, due to lower interfacial tension. Shorter formation times are observed at larger Q_d, as opposed to drop diameter. The above results are compared with the numerical simulations and good agreement is found, with an average error of 0.8 % for d/l_c and 2.4 % for $\tilde{t}$. The HSI experiments also agreed well with the μPIV results, as seen from figure 3 with an error below 1 %.

Moreover, a prediction of the drop size was obtained by using a data-driven model (Chagot *et al.* 2022). As discussed by Kalli *et al.* (2022), the dynamic interfacial tension should be used to obtain accurate drop size predictions, but it is difficult to be obtained experimentally. For this reason, CFD should preferably be used to estimate the droplet volume in the presence of surfactants. Alternatively, data-driven models can also be used if there is a large database available.

4. Results and discussion

The vortical structures and the velocity fields obtained from the CFD simulations and the high-speed μPIV experiments in surfactant-free and surfactant-laden systems, as well as the concentration profiles in the bulk and at the interface are discussed here, for all stages of the drop formation process. The results for the surfactant-free case will be discussed first to show the spatio-temporal evolution of the interface, as well as the vortical structures during each stage. In addition, the surfactant concentrations in the bulk and at the interface for the various stages of drop formation will be discussed based on the CFD simulations.

4.1. *Surfactant-free case*

The spatio-temporal evolution of the interface during the complete drop formation process was first simulated for the surfactant-free case. Figure 4 shows the changes in the shape of the interface during expansion (*a*), necking (*b*) and pinch-off (*c*) for $Q_d = 0.02$ and $Q_c = 0.12\,\mathrm{ml\,min^{-1}}$. A different output time step is used for each stage equal to 1, 0.5, and 0.1 ms, respectively, with the longest one used for the expansion stage and the shortest for pinch-off. Specifically, the evolution of the interface is slow during expansion, becomes moderately rapid during necking and very rapid just before pinch-off. In previous work, expansion times were also found to be longer compared with necking ones, for both surfactant-free and surfactant-laden cases in the dripping regime (Kalli & Angeli 2022). A similar trend was seen by Kahouadji *et al.* (2018) for pancake-shaped drops. The vortical structures inside the drop are shown in figure 4(*d*) for the expansion and necking stages and in figure 4(*e*) for pinch-off. The velocity fields from the experiments with and without surfactant are shown in figure 5, which agree very well with the simulation results. Initially for the surfactant-free case (at $\tilde{C} = 0$ and $\tilde{t} = 0.10$, figure 4*d*), two vortical structures are seen close to the front of the drop which grow larger and move closer to the interface later on (at $\tilde{t} = 0.50$). This is in agreement with the experimental results, where large internal circulation patterns are observed in expansion at $\tilde{t} = 0.10$ and $\tilde{t} = 0.50$ (figure 5(*a*,*b*) respectively). The circulation pattern is more pronounced in the second stage of expansion ($\tilde{t} = 0.50$, figure 5*b*), where two circulation zones are clearly seen, one on each side of the growing drop and high velocities in the middle, reaching a maximum of $|U_{max}|/U_{sc} = 0.45$. From the shape of the interface (black dotted line) it is clear that originally the drop grows in the radial direction, as the continuous phase obstructs the flow of the dispersed phase. The high velocities on the sides of the dispersed phase during expansion suggest that the liquid is mainly transported through the sides of the drop. This is in agreement with observations reported previously by several authors (Pirbodaghi *et al.* 2015; Roumpea *et al.* 2019). Previous works using ghost particle velocimetry in rectangular flow-focusing microchannels reported a stagnation point at the base of the growing drop, during the second stage of expansion, but no significant circulation in the surfactant-free case (Kiratzis *et al.* 2022). Even though a stagnation point can be seen in this work during the second stage of expansion (figure 5*e*), the presence of the strong circulation can be attributed to the higher flow rates used in this study and the differences in

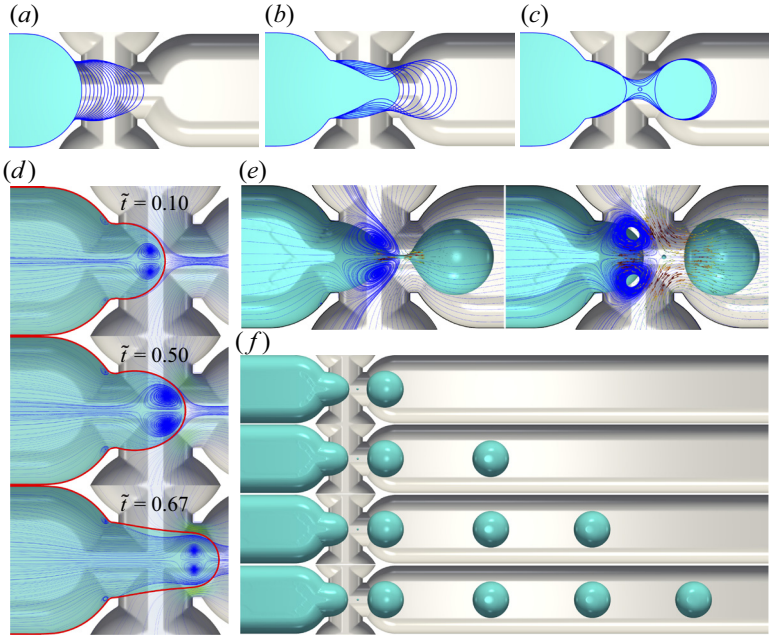

Figure 4. Numerical results for the surfactant-free case generated with $Q_d = 0.02$ and $Q_c = 0.12$ ml min. (*a–c*) Depict the spatio-temporal evolution of the interface with time differences between the curves of 1, 0.5 and 0.1 ms, respectively; (*d*) highlights the vortical structures for three different times that can also be compared with experimental PIV of figure 5(*a–c*) (shown in red lines); (*e*) shows the development of a neck followed by pinch-off which is accompanied by satellite formation; (*f*) shows top views of the periodic drop formation in the channel with a period of 13.5 ms.

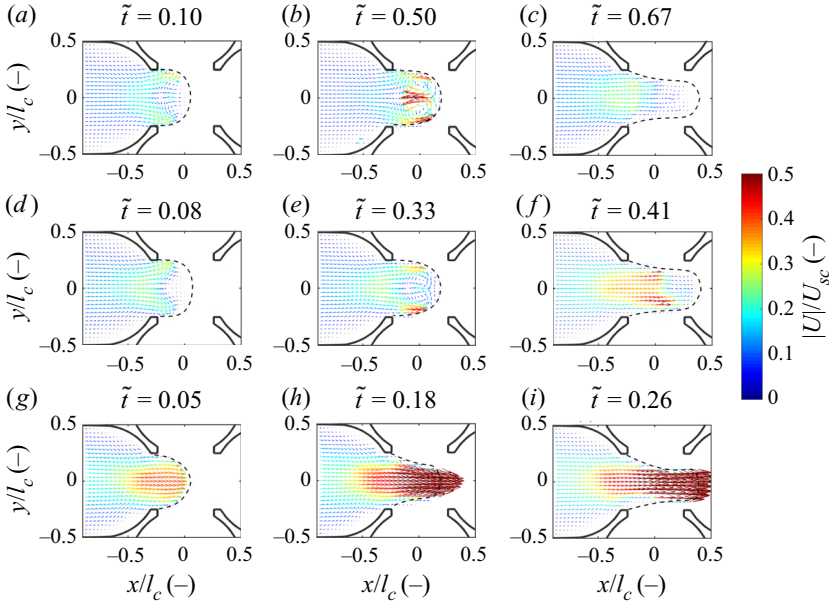

Figure 5. Effect of TX100 concentration on velocity fields from PIV measurements during expansion and necking stages at $Q_d = 0.02$ ml min^{-1} for (*a–c*) $\tilde{C} = 0$, (*d–f*) $\tilde{C} = 0.06$ and (*g–i*) $\tilde{C} = 2.89$.

microchannel geometries. In rectangular channels, there is corner flow in the gutters of the channel, which is absent in the current work where the channels have an oval cross-section. The gutter flow can also reverse the direction of the flow fields after the drop has formed (Mießner *et al.* 2020; Kovalchuk & Simmons 2021).

As the drop grows, it obstructs the inlet of the oil phase, which now pushes the interface perpendicular to the drop and changes its curvature. This marks the beginning of the necking stage, with the neck defined as the bridge between the growing drop and the dispersed phase remaining attached to the inlet. The curvature of the interface becomes negative and the pressure build-up from the continuous phase causes the flow to be higher in the neck compared with the rest of the dispersed phase (with $|U_{max}|/U_{sc} = 0.25$), while the velocities near the interface decrease. In addition, the vortical structures decrease in size ($\tilde{t} = 0.67$ in figures 4(*d*) and 5(*c*)). This indicates that the transport of the dispersed phase from the sides is significantly weaker than in the expansion stage. As the process approaches pinch-off (see figure 4(*e*), left panel), large vortical structures form in the region of the dispersed phase that remains attached to the inlet. Immediately after the pinch-off, the vortical structures grow large in the middle of the cross-junction (figure 4(*e*), right panel). This vortex dipole just before and at pinch-off was also observed during the formation of surfactant-free plugs (Kahouadji *et al.* 2018). Another agreement between the two works is the stagnation point present just at the location of pinch-off. A small satellite drop is also seen at the point where the neck broke. The distance between four subsequent drops is equal, as shown in figure 4(*f*), indicating that the drop formation process is periodic with exactly the same formation time of 13.5 ms in each cycle.

4.2. *Surfactant-laden cases*

4.2.1. *Expansion and necking stages*

Upon addition of the TX100 surfactant at $\tilde{C} = 0.06$, the velocity fields change significantly from their surfactant-free counterparts throughout all stages of the drop formation process. At the start (see figure 5(*d*) at $\tilde{t} = 0.08$), the average velocities appear higher and more uniform at the back of the forming drop and a less intense circulation pattern can be seen in the centre. The two circulation zones still appear in the second phase of the expansion stage (see figure 5(*e*) at $\tilde{t} = 0.33$), however, their velocities are lower than in the surfactant-free case. During the necking stage at TX100 concentrations below CMC (figure 5*f*), higher velocities are observed near the neck, with maximum values of $|U_{max}|/U_{sc} = 0.45$. The reduced interfacial tension due to the presence of surfactant accelerates the neck thinning and results in high velocities (figure 5(*f*) at $\tilde{t} = 0.41$), as also observed by Kiratzis *et al.* (2022). The circulation pattern completely disappears during necking at low TX100 concentrations, which agreed with the CFD simulations. For concentrations above the CMC, during the first expansion phase (see figure 5(*g*) at $\tilde{t} = 0.05$), velocities are high inside the whole of the growing drop, reaching a maximum of $|U_{max}|/U_{SC} = 0.4$. Velocities then increase significantly as shown in figure 5(*h–i*) as the drop expands into the main channel, and at the necking stage at $\tilde{t} = 0.18$ and 0.26, reaching a $|U_{max}|/U_{sc} = 0.5$.

4.2.2. *Pinch-off*

Pinch-off is further discussed in this section, using both the numerical and experimental results. The effect of TX100 surfactant on drop shape and velocity fields at pinch-off from HSI and μPIV experiments, as well as CFD simulations at $Q_d = 0.02\,\mathrm{ml\,min^{-1}}$ as shown in figure 6. As can be seen in figure 6(*a*,*d*,*g*), smaller droplets are formed upon TX100

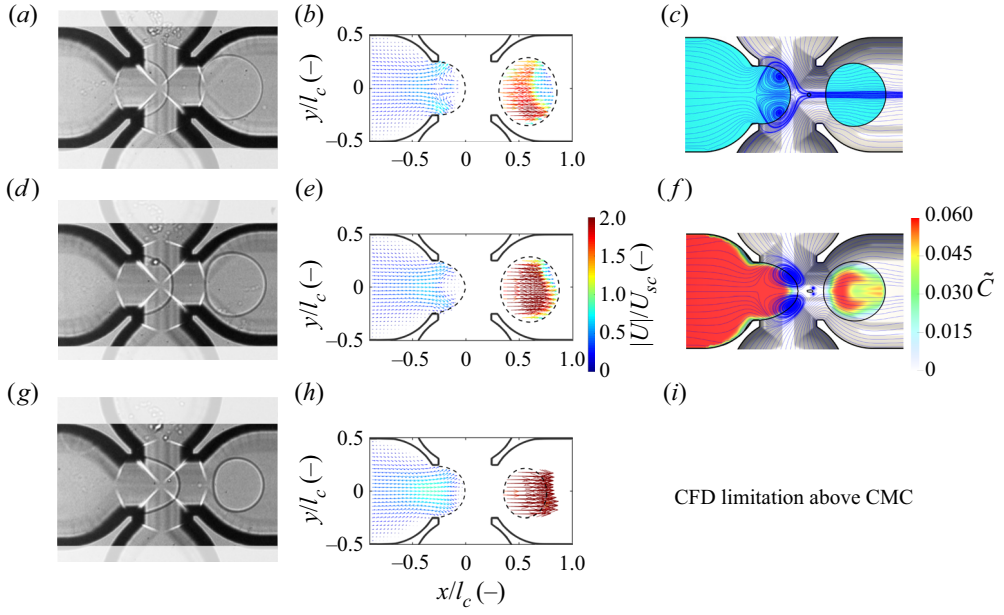

Figure 6. Effect of TX100 concentration on velocity fields from HSI experiments (*a*,*d*,*g*), PIV measurements (*b*,*e*,*h*) and CFD (*c*,*f*,*i*) at the pinch-off point for $0.02\,\mathrm{ml\,min^{-1}}$ for (*a–c*) $\tilde{C} = 0$, (*d–f*) $\tilde{C} = 0.06$ and (*g–i*) $\tilde{C} = 2.89$.

addition and satellite drops are seen after pinch-off. It should be noted that the shadow from the edge of the channel observed when using HSI does not exist in the μPIV images, which can mislead the comparison of the droplet sizes in figure 6(*c*,*f*). In the case of no surfactant present, high velocities at the rear of the formed drop and circulation patterns in the dispersed phase remaining attached to the inlet are seen in figure 6(*b*,*c*) (see also figure 4). The higher velocities at the rear of the drop, as opposed to its front, are also observed in the surfactant-free simulations of Zhao *et al.* (2015). Similar observations were reported from CFD simulations of mass transfer in a flow-focusing microchannel by Lan *et al.* (2014).

When surfactant is added at concentrations below CMC, smaller droplets form due to the lower interfacial tension, and a weaker circulation pattern is seen at the remaining dispersed phase. The velocities inside the formed droplet are higher compared with the surfactant-free case (figure 6(*e*,*f*) at $\tilde{C} = 0.06$). A stagnation point is also observed in the CFD output just at pinch-off for both surfactant-free and surfactant-laden cases. At concentrations above the CMC, the experimental μPIV results show that the circulation pattern completely disappears and uniform velocity fields are observed in the formed droplet, with $|U_{max}|/U_{sc} = 0.5$ (figure 6(*h*) at $\tilde{C} = 2.89$). As was discussed above, the model does not account for micelle formation, and no numerical results are shown for concentrations above CMC.

4.2.3. *Concentration distribution*

Figure 7 shows the relative bulk concentration of the TX100 surfactant (*a*), $\tilde{C}$, the vortical structures (*b*) and the interfacial concentration (*c*), ($\tilde{\Gamma}$), during the drop formation process at concentrations below CMC ($\tilde{C} = 0.06$). The concentration profile of the surfactant in

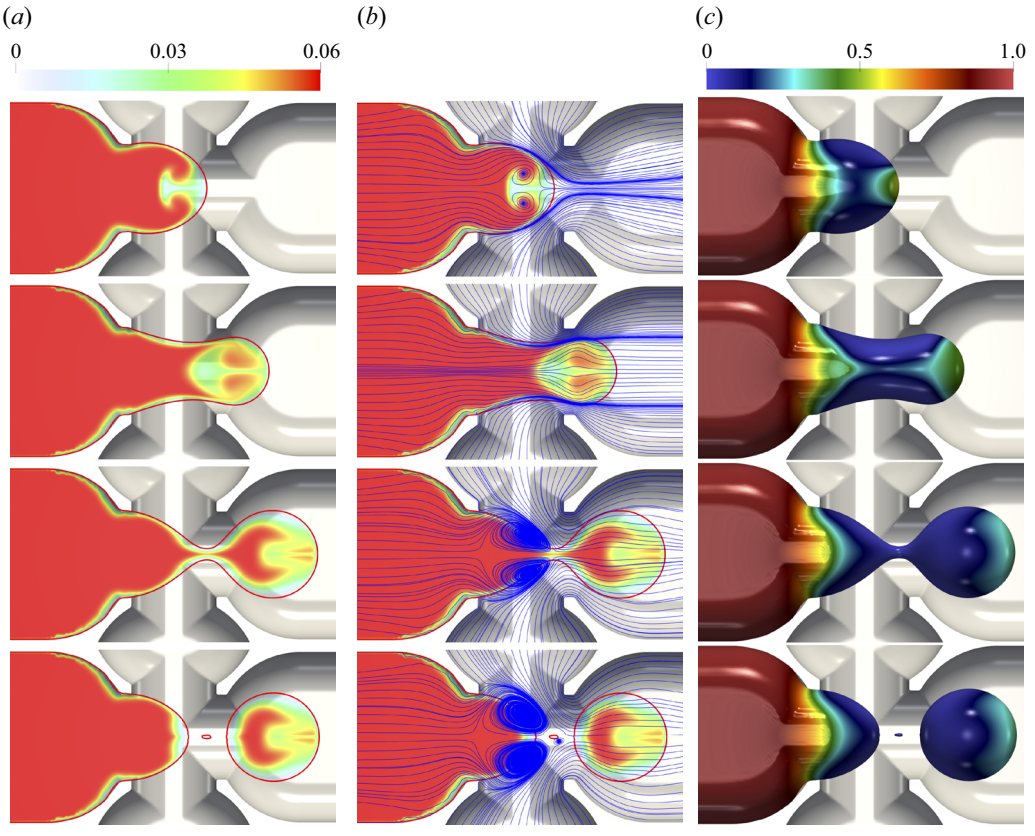

Figure 7. Spatio-temporal evolution of (*a*) the relative bulk surfactant concentration $\tilde{C}$, (*b*) the vortical structures in the channel reference frame and (*c*) the relative interfacial surfactant concentration $\tilde{\Gamma}$, respectively. The snapshots from top to bottom correspond to times $\tilde{t} = 0.39$, 0.78, 0.98 and 0.99, respectively, and $\tilde{C} = 0.06$.

the bulk follows the circulation patterns as seen in the expansion stage ($\tilde{t} = 0.39$, top of figure 7*a*,*b*). During the necking stage, the circulation is weaker and the surfactant transfers downstream, following the drop growth and into the main channel ($\tilde{t} = 0.78$). Just before pinch-off, the two circulation zones in the drop disappear and the concentration of surfactant is high at the rear of the drop ($\tilde{t} = 0.98$). Large circulation patterns appear at the front of the phase remaining attached to the inlet, which grow larger after drop detachment ($\tilde{t} = 0.99$). Interestingly, the small satellite drop appears to have no surfactant. As also observed in the μPIV experiments, the circulation zones in all stages are smaller compared with the surfactant-free case. This is possibly due to Marangoni forces acting in the opposite direction to the circulation when surfactant is present.

As previously discussed, information on the surfactant concentration at the interface is paramount in understanding the effect of TX100 on the drop formation process. The spatio-temporal evolution of the relative interfacial concentration ($\tilde{\Gamma}$) is shown in figure 7(*c*). As can be noticed, the interfacial concentration of the surfactant is high (and equal to the equilibrium value) at the left part of the channel, and before the cross-junction where the interface forms. At the interface there is initially very little surfactant concentration, apart from the tip of the drop. Even at the tip, however, the concentration is below the equilibrium value. This concentration profile remains at

all stages of the formation process, including expansion (top), necking (middle) and pinch-off (bottom). The difference in surfactant concentration along the interface will cause Marangoni stresses that can affect the drop formation time and the velocity fields inside the drop; this will be discussed further in § 4.2.4.

4.2.4. *Marangoni stresses*

Marangoni stresses are usually discussed in works for drop coalescence (Dong *et al.* 2019; Constante-Amores *et al.* 2021*a*), rising bubbles (Bastani *et al.* 2018), liquid bridges (Kovalchuk, Nowak & Simmons 2017; Kamat *et al.* 2018) and jet formation (Antonopoulou *et al.* 2021), but less frequently during the fast process of drop formation. In this section, Marangoni stresses at the interface will be calculated and presented as a function of time, space and dispersed phase flow rate for the first time during the whole drop formation process. Additionally, the competition between Marangoni stresses and the interfacial tension reduction caused by the surfactant absorption will be explored in all dimensions of the forming drop.

Figure 8 shows the shape of the interface and the dimensionless interfacial concentration of surfactant during drop formation, with the magnitude of $\tilde{\Gamma}$ shown in colour in (*a*,*b*) for top (*x*–*y* plane) and side (*x*–*z* plane) views, respectively. The corresponding local interfacial tension (σ/σ_s) and the Marangoni stress ($\boldsymbol{\nabla}(\sigma/\sigma_s)\cdot\boldsymbol{t}$) are shown in figures 8(*c*,*d*) and 8(*e*,*f*), respectively. The 3 profiles represent the expansion stage at $\tilde{t}=0.39$, the initial part of the necking stage at $\tilde{t}=0.78$ and the final part of necking before pinch-off at $\tilde{t}=0.98$, for $Q_d=0.02$ and $Q_c=0.12\,\mathrm{ml\,min^{-1}}$. The concentration gradient at the interface decreases as the drop grows, with the concentration at the drop tip reaching a maximum of $\tilde{\Gamma}=0.58$ at $\tilde{t}=0.39$, which decreases to $\tilde{\Gamma}=0.48$ at $\tilde{t}=0.78$ and $\tilde{\Gamma}=0.35$ at $\tilde{t}=0.98$ (as also seen in figure 7*c*). This causes a weaker interfacial tension gradient for the top view as observed from the slope in figure 8(*c*) which decreases as the drop forms. The Marangoni stresses on the interface are small and in the opposite direction to the flow, as seen from the negative peaks in figure 8(*e*) with $\boldsymbol{\nabla}(\sigma/\sigma_s)=-2.4$, -0.7 and -0.3 at $\tilde{t}=0.39$, 0.78 and 0.98 respectively ($0.4<x/l_c<1.2$). The positive peak in the direction of the forming drop, around $x/l_c=0$ in the range of $0.0<x/l_c<0.2$ with $\boldsymbol{\nabla}(\sigma/\sigma_s)\cdot\boldsymbol{t}\sim 1.5$ exists for all three stages, but is far from the neck region to contribute to pinch-off.

The flow of the continuous phase from both the top and bottom inlets ($Q_c=0.12\,\mathrm{ml\,min^{-1}}$) is high enough to sweep surfactant molecules away from the neck towards both sides of the neck and results in an essentially surfactant-free interface at the neck region. The depletion of surfactant in the neck area in the range $0.2<x/l_c<0.9$ (as also seen in figure 7*c*) and the flat concentration profile of $\tilde{\Gamma}$ shows that there are no Marangoni stresses to affect the process of pinch-off. The shorter drop formation times observed when surfactants are present are caused by the lower interfacial tension compared with the surfactant-free case. The effect of this dominates over Marangoni stresses as the high continuous phase flow rate cleans the interface during the whole formation process (see figure 8). The maximum in $\tilde{\Gamma}$ at all times close to the drop tip causes local Marangoni stresses in that area whose strength decreases with time. These stresses slow down the velocity inside the drop and weaken the circulation intensity (as discussed in § 4.2) rather than delay pinch-off. This is opposite to the case of jet formation where Marangoni stresses delay break-up and result in longer times to pinch-off (Kalli & Angeli 2022). Additionally, the presence of surfactant in both stages of expansion (side view in figure 8*b*) can justify the lower times observed during expansion in the surfactant-laden cases (figure 5*d*,*e*,*g*,*h*), as opposed to the surfactant-free experiments (figure 5*a*,*b*). Thus, it can be inferred that the

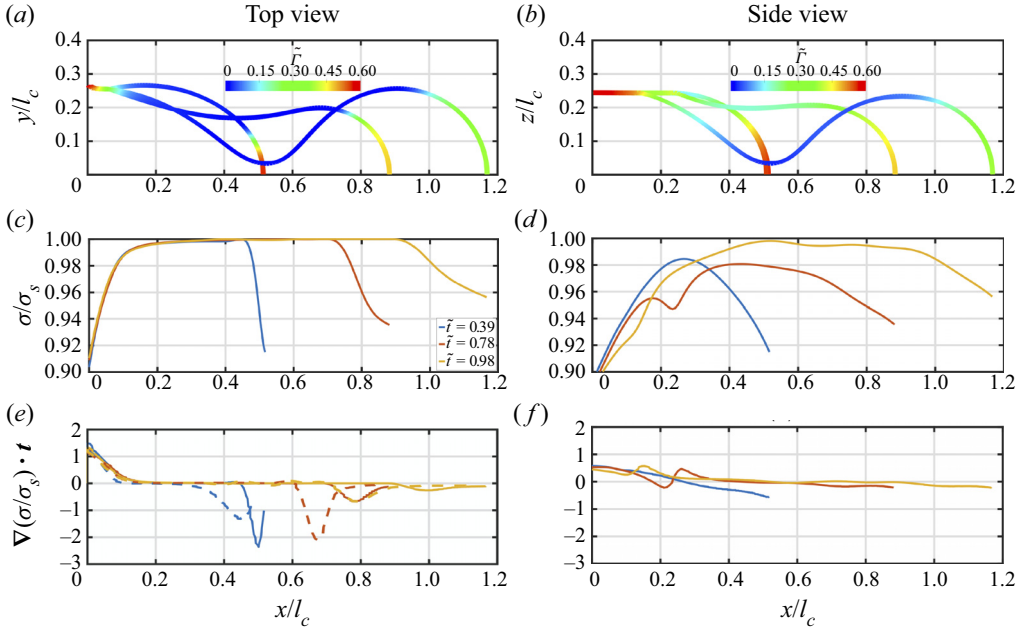

Figure 8. Quantitative measures highlighting (*a*,*b*) the interface shape and the interfacial surfactant distribution with the magnitude of Γ/Γ_∞ shown in colour, (*c*,*d*) the corresponding local interfacial tension σ/σ_s and (*e*,*f*) the Marangoni stress $\nabla(\sigma/\sigma_s) \cdot \boldsymbol{t}$, for top and side views, respectively. The dashed lines in (*e*) correspond to $Q_d = 0.01\ \mathrm{ml\ min^{-1}}$ at equivalent times in each stage.

expansion stage leads the drop formation process (Kalli & Angeli 2022) and is the main contributor in decreasing the formation time in the surfactant-laden cases, as opposed to necking and pinch-off.

The Marangoni stresses were also calculated for a lower dispersed phase flow rate ($Q_d = 0.01\ \mathrm{ml\ min^{-1}}$), as shown with dashed lines in figure 8(*e*). As it can be seen, at a lower dispersed phase flow rate, the Marangoni stresses are lower during expansion but higher during necking compared with the $Q_d = 0.02\ \mathrm{ml\ min^{-1}}$ case. However, in both cases the Marangoni stresses are low, with $\nabla(\sigma/\sigma_s) \cdot \boldsymbol{t} = 0.8$ for $Q_d = 0.01\ \mathrm{ml\ min^{-1}}$ and $\nabla(\sigma/\sigma_s) \cdot \boldsymbol{t} = 0.3$ for $Q_d = 0.02\ \mathrm{ml\ min^{-1}}$ and away from the pinch-off point. In fact, just at the pinch-off location ($x/l_c = 0.5$), $\nabla(\sigma/\sigma_s) \cdot \boldsymbol{t} = 0$, which confirms that Marangoni stresses do not contribute to the pinch-off point at the conditions studied in this work.

The influence of the continuous phase flow rate on the surfactant distribution at the interface is obvious when the top and side views are compared. The surfactant concentration distribution at the interface is less uniform in the side than in the top view, while the neck area has some surfactant, apart from the last part of the necking stage (figure 8*b*). This results in a lower interfacial tension overall, which will contribute to the decrease in drop formation time. Marangoni stresses now appear with peaks close to the neck region in the range $0.1 < x/l_c < 0.3$ at $\tilde{t} = 0.78$ and $0.1 < x/l_c < 0.2$ at $\tilde{t} = 0.98$. Nonetheless, their magnitude is small ($\nabla(\sigma/\sigma_s) \cdot \boldsymbol{t} < 1$) and they are not close to the thinning part of the neck ($0.4 < x/l_c < 0.6$ at $\tilde{t} = 0.98$) so should not contribute to pinch-off. As seen in the literature for liquid threads and jets, the presence of surfactant does not alter the classic scaling laws of pinch-off (Craster, Matar & Papageorgiou 2002; Wee *et al.* 2021). The surfactant is convected away from the thread neck by the capillary-driven flow and the influence of Marangoni stresses on pinch-off is negligible

(Kamat *et al.* 2018). In this work where drop formation is studied, the flow from the continuous phase also pushes away the surfactant from the neck region, and the pinch-off is found to be unaffected by Marangoni stresses.

Antonopoulou *et al.* (2021) compared experimental results with numerical simulations of a weak ($\beta_s = 0.1$, identical to this study) and a strong ($\beta_s = 1$) surfactant during jet formation and break-up. It was found that the distribution of the weak surfactant at the interface was less uniform as opposed to the strong surfactant. It was also found that surfactant concentration gradients and thus Marangoni stresses decrease progressively with time during the formation process of jets, as seen in this work for drop formation.

4.3. *Fully formed drops*

In order to investigate surfactant transport in the whole drop volume, the vortical structures and surfactant concentrations of the formed drops as obtained by the CFD simulations are shown in figure 9 for surfactant-laden (*c–h*) cases after pinch-off (at the end of the channel, $10 \times d$). The vortical structures for surfactant-free drops are shown in figure 9(*a*,*b*) for comparison. The difference in the shape of the formed drop for top-(*a*,*c*,*e*,*g*) and side-(*b*,*d*,*f*,*h*) views is due to the channel dimensions, as explained in §§ 2 and 3. In the surfactant-free case, the vortical structures are completely symmetrical from the top view, while a strong vortex dipole is seen from the side view near the rear boundaries of the drop. In the surfactant-laden case at $\tilde{C} = 0.006$ (*c*,*d*), the vortical structures remain symmetrical from the top view and the vortex dipole moves towards the centre of the drop from the side view. The opposite is seen at higher surfactant concentrations ($\tilde{C} = 0.06$, *e*,*f* and $\tilde{C} = 0.2$, *g*,*h*); a strong vortex dipole is forming in the centre of the top view, while no circulation is seen in the side view.

Both bulk and interfacial concentrations of the formed drops are plotted in figure 9 for $\tilde{C} = 0.006$ (*c*,*d*), $\tilde{C} = 0.06$ (*e*,*f*) and $\tilde{C} = 0.21$ (*g*,*h*) in their dimensionless form as $\tilde{C}$ and $\tilde{\Gamma}$, respectively. At the very low concentration ($\tilde{C} = 0.006$), most of the surfactant is at the interface (maximum value of $\tilde{\Gamma} = 0.5$) and there is almost no surfactant in the bulk (maximum value of $\tilde{C} = 1.7 \times 10^{-4}$). For the higher concentration cases at $\tilde{C} = 0.06$ and $\tilde{C} = 0.21$, the surfactant concentration is high in the centre and low around the periphery of the drop in both the top and side views. The variations in $\tilde{\Gamma}$ are small, as can be seen from the range of the scale in the figure. Here it should be noted that adsorption is significantly faster than desorption, as also expected from the large $K_L = 1585.00\,\mathrm{m^3\,mol^{-1}}$ value. As mentioned in § 3, $Bi = 8.41 \times 10^{-5}$ is very small, which can be considered negligible when compared with $k = 5.55 \times 10^3$, denoting negligible desorption as opposed to adsorption of surfactant at the interface. When compared with the concentrations during drop formation, it is obvious that the surfactant absorbs very fast after pinch-off. As seen in figure 7, the bulk concentration reaches the maximum value inside the drop throughout all stages ($\tilde{C} = 0.06$) and the interface is not saturated ($\tilde{\Gamma} < 1$). This is not the case for fully formed drops, where the bulk concentration is lower than the maximum value. However, there are some differences in the interfacial concentration of the surfactant. From the top view, $\tilde{\Gamma}$ is seen to be higher at the rear of the drop. On the other hand, the interfacial concentration of the surfactant is larger near the rear edges of the drop from side view, especially in the $\tilde{C} = 0.21$ case. This is due to advection of surfactant at the back of the drop as it travels through the channel. The average concentrations in the bulk and at the interface just after pinch-off (t^+), were calculated by integrating over the drop volume and surface area, respectively. These concentrations

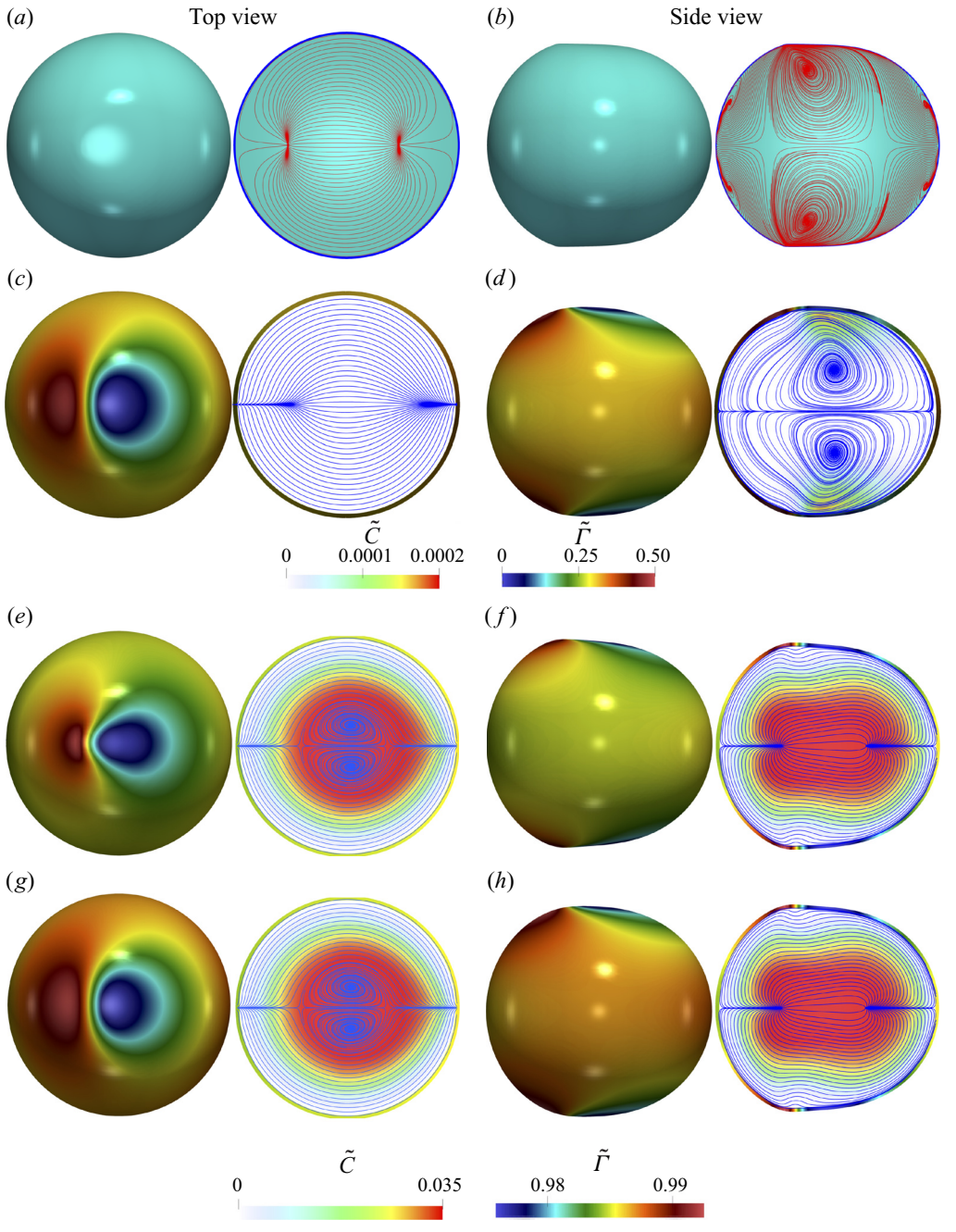

Figure 9. Top and side views of resulting drop for the surfactant-free case (*a*,*b*) and surfactant-laden case (*c*–*h*) accompanied by their vortical structures in the moving reference frame. All cases are for $Q_d = 0.02$, $Q_c = 0.12\,\mathrm{ml\,min^{-1}}$. The panel from top to bottom corresponds to surfactant free (*a*,*b*), $\tilde{C} = 6 \times 10^{-3}$ (*c*,*d*), $\tilde{C} = 6 \times 10^{-2}$ (*e*,*f*) and $\tilde{C} = 0.21$ (*g*,*h*). These surfactant-laden conditions correspond to the non-dimensional parameters: $Re = 2.35$, $Ca = 4.33 \times 10^{-3}$, $Pe_c = Pe_d = 2.35 \times 10^5$, $Bi = 8.41 \times 10^{-5}$ and $k = 5.55 \times 10^3$.

Q_d	$C(t^+)/C_{ini}$	$\Gamma(t^+)/\Gamma_{ini}$
0.01 ml min^{-1}	55 %	37 %
0.02 ml min^{-1}	60 %	30 %

Table 2. Concentrations in the formed drop after pinch-off.

were compared with the initial values, C_{ini} and Γ_{ini}. Table 2 summarises the calculated ratios for $Q_d = 0.01$ and $Q_d = 0.02$ ml min^{-1}. At $Q_d = 0.01$ ml min^{-1} it was found that 55 % of the initial bulk concentration remains in the drop after pinch-off ($C(t^+)/C_{ini}$) and 37 % ($\Gamma(t^+)/\Gamma_{ini}$) from the initial interfacial concentration is at the interface, for all bulk concentrations ($\tilde{C} = 0.006$, 0.06 and 0.21). These values change to $C(t^+)/C_{ini} = 60$ % and $\Gamma(t^+)/\Gamma_{ini} = 30$ % at $Q_d = 0.02$ ml min^{-1}. The higher interfacial concentration value in the former case is due to the longer formation time at $Q_d = 0.01$ ml min^{-1} (see figure 3), allowing more time for the surfactant to travel to the interface.

5. Conclusions

This paper presents a thorough study of the formation process of surfactant-laden drops inside a flow-focusing microchannel. High-speed imaging experiments and novel μPIV experiments were used in conjunction with numerical CFD simulations, to obtain velocity and surfactant concentration profiles and understand the effects of surfactants on the different stages of the drop formation process. Surfactant concentrations below and above the CMC were considered. The numerical simulation utilised a three-dimensional multiphase solver which accounted for the transport of soluble surfactants in the bulk and at the interface and was adapted to the context of the hybrid front-tracking/level-set method.

A low-viscosity silicone oil (4.6 mPa s) was used as the continuous phase and a mixture of 48 % w/w water and 52 % w/w glycerol was the dispersed phase. A non-ionic surfactant ($\text{CMC}_{TX100} = 3.5$ mM) was added in the aqueous phase, at several concentrations below and above CMC. Numerical simulations for the drop formation in the microfluidic channel showed good agreement with experiments on drop size, formation time and vortical structures during drop formation.

Results revealed smaller dimensionless drop size (d/l_c) and shorter formation times ($\tilde{t}$) at higher surfactant concentrations ($\tilde{C}$) in the drop bulk due to the lower interfacial tension forces. During the drop expansion and necking stages, velocities at the back of the forming drop were higher at higher $\tilde{C}$ values while the circulation patterns completely disappeared at concentrations above the CMC. At the pinch-off point, the velocities were higher at the rear of the drop as opposed to the front, while circulation patterns in the dispersed phase remaining attached to the inlet were weaker when surfactant was added compared with the cases with no surfactant. The effect of the dispersed phase flow rate was also investigated and it was found that an increase in flow rate resulted in less surfactant at the interface, due to shorter formation times.

The surfactant concentrations in the bulk and at the interface of the formed drop were also explored. Marangoni stresses at the drop interface were calculated for all stages of drop formation and found to progressively weaken with formation time. It was concluded that the high continuous phase flow rate plays an important role in sweeping surfactants away from the neck region and contributed towards pinch-off mainly. The Marangoni stresses did not seem to affect the neck pinch-off but contributed mainly to the velocity

profile inside the drop, as opposed to what has been found in previous jet formation and break-up studies. Instead, the main contributor to the decreased formation time in the surfactant-laden cases was found to be the Marangoni stresses that develop during the expansion stage ($Q_d = 0.02\,\mathrm{ml\,min^{-1}}$) and the necking stage ($Q_d = 0.01\,\mathrm{ml\,min^{-1}}$). These stresses suppress circulation and increase the velocities inside the forming drop, which accelerate the formation and result in lower formation times overall (figure 5).

In future work, a new experimental set-up will be developed using micro-laser induced fluorescence techniques to trace both time and spatial evolutions of the surfactant concentration at the interface and compare with numerical results. Additionally, the numerical simulations will be expanded to model concentrations above CMC by accounting for micelle formation.

Funding. This work is supported by the Engineering and Physical Sciences Research Council, UK, through the EPSRC MEMPHIS (EP/K003976/1) and PREMIERE (EP/T000414/1) programme grants. M.K. would like to acknowledge the EPSRC doctoral training programme (EP/ R513143/1) for her studentship. O.K.M. acknowledges funding from PETRONAS and the Royal Academy of Engineering for a research chair in multiphase fluid dynamics. P.P. and L.K. acknowledge HPC facilities provided by the Research Computing Service (RCS) of Imperial College London for the computing time. D.J. and J.C. acknowledge support through HPC/AI computing time at the Institut du Developpement et des Ressources en Informatique Scientifique (IDRIS) of the Centre National de la Recherche Scientifique (CNRS), coordinated by GENCI (Grand Equipement National de Calcul Intensif) grant 2022 A0122B06721. The numerical simulations were performed with code BLUE (Shin *et al.* 2017, 2018) and the visualisations were generated using ParaView.

Declaration of interests. The authors report no conflict of interest.

Author ORCIDs.
M. Kalli https://orcid.org/0000-0001-8741-0587;
L. Chagot https://orcid.org/0000-0002-7467-4855;
L. Kahouadji https://orcid.org/0000-0001-8805-1192;
S. Shin https://orcid.org/0000-0002-9196-3966;
J. Chergui https://orcid.org/0000-0002-1578-6435;
D. Juric https://orcid.org/0000-0003-3703-0601;
O.K. Matar https://orcid.org/0000-0002-0530-8317;
P. Angeli https://orcid.org/0000-0001-9575-4259.

Appendix A. Inlet velocity profile

The cross-section of the three inlets is comprised two main areas: two semi-circles of radius $R = w_c/2$ and a rectangular portion of dimensions $w_c \times (l_c - w_c)$. The coordinates of centre point of the cross-section are defined as x_0 and y_0, and the distance in the x-axis from the edge of the rectangular portion to the centre line as $L = (l_c - w_c)/2$. We begin with a general parabolic function consistent with a Poiseuille profile for the velocity at the rectangular portion ($f_1(x, y)$)

$$f_1(x, y) = a_1(x - x_0)^2 + b_1(y - y_0)^2 + c_1 \quad \text{if } (x - x_0) \in [-L, L], \tag{A1}$$

where a_1, b_1 and c_1 are constants. Applying a no-slip condition at the channel walls ($f_1(x, \pm R) = 0$) and considering symmetry across the x-axis, we obtain $a_1 = 0$ and $b_1 = -c_1/R^2$:

$$f_1(x, y) = -\frac{c_1}{R^2}(y - y_0)^2 + c_1. \tag{A2}$$

We define the parabolic profile for the circular sections in cylindrical coordinates ($f_2(r, \theta)$)

$$f_2(r, \theta) = a_2(L + \sin\theta)^2 + b_2(r\cos\theta)^2 + c_2 \quad \text{if } (x - x_0) \leqslant -L \text{ or } (x - x_0) \geqslant L, \tag{A3}$$

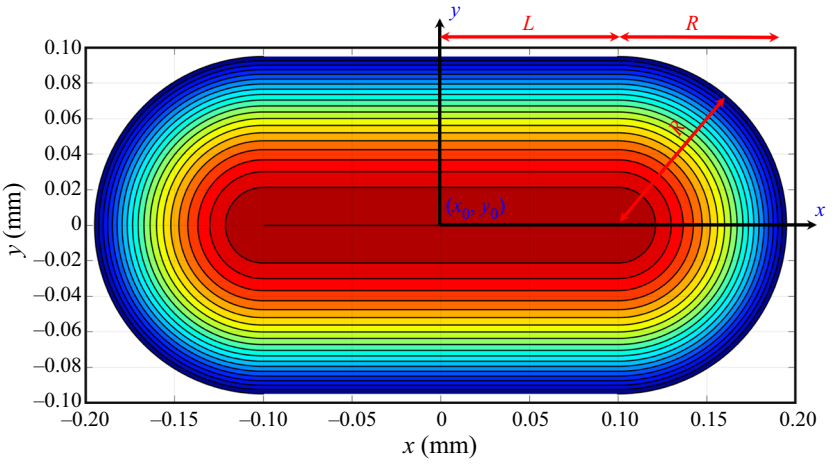

Figure 10. Normalised inlet velocity profile. The contours are equally spaced with steps of 0.05 and $(x_0, y_0) = (0, 0)$.

where $x - x_0 = L + \sin\theta$ and $y - y_0 = r\cos\theta$. Applying a continuity condition at the limit between the rectangular and circular sections, $\partial f_1/\partial y|_{x-x_0=L} = \partial f_2/\partial r|_{\theta=0,\pi}$, as well as the no-slip condition at the walls, $f_2(\theta, R) = 0$, we obtain $b_2 = b_1 = -c_1/R^2$ and $c_1 = c_2$

$$f_2(r,\theta) = -\frac{-c_1}{R^2}(\sin\theta)^2 - \frac{c_1}{R^2}(r\cos\theta)^2 + c_1 \quad \text{if } (x - x_0) \leqslant -L \text{ or } (x - x_0) \geqslant L. \tag{A4}$$

Considering symmetry across the θ-axis

$$f_2(r) = \frac{c_1}{R^2}(r\cos\theta)^2 + c_1 \quad \text{if } (x - x_0) \leqslant -L \text{ or } (x - x_0) \geqslant L. \tag{A5}$$

These profiles must satisfy the exact entry flow rate of each branch. Therefore, we refer to the definition of flow rate Q in order to find constant c_1

$$\left.\begin{aligned} Q &= \int_{-R}^{R}\int_{-L}^{L} f_1(x,y)\,\mathrm{d}x\,\mathrm{d}y + 2\int_0^{\pi}\int_0^{R} f_2(r) r\,\mathrm{d}r\,\mathrm{d}\theta, \\ c_1 &= -\frac{Q}{\dfrac{8}{3}RL + \dfrac{\pi}{2}R^2}. \end{aligned}\right\} \tag{A6}$$

Replacing the value of c_1 on (A2) and the cartesian version of (A5), we obtain the inlet velocity profile for the cross-section considered in this study, illustrated in figure 10

$$\boldsymbol{u}(x,y) = \begin{cases} \mathcal{A}\left(\dfrac{(y-y_0)^2}{R^2} - 1\right) & \text{if } |x - x_0| \leq L \\ \mathcal{A}\left(\dfrac{(x-x_0-L)^2}{R^2} + \dfrac{(y-y_0)^2}{R^2} - 1\right) & \text{otherwise,} \end{cases} \tag{A7}$$

where $\mathcal{A} = -Q/(\frac{8}{3}RL + (\pi/2)R^2)$.

References

Aicolina, L.E., Leaver, I.H. & Stapleton, I.W. 1989 Fluorescence quenching studies of the self-association in ater of fluorescent surfactants. Alkaryl-2-pyrazolines and alkyl-7-hydroxycoumarins. *Dyes Pigments* **11** (3), 213–232.

Antonopoulou, E., Harlen, O.G., Rump, M., Segers, T. & Walkley, M.A. 2021 Effect of surfactants on jet break-up in drop-on-demand inkjet printing. *Phys. Fluids* **33** (7), 72112.

Bastani, D., Fayzi, P., Lotfi, M. & Arzideh, S.M. 2018 CFD simulation of bubble in flow field: investigation of dynamic interfacial behaviour in presence of surfactant molecules. *Colloid Interface Sci. Commun.* **27**, 1–10.

Batchvarov, A., Kahouadji, L., Magnini, M., Constante-Amores, C.R., Shin, S., Chergui, J., Juric, D., Craster, R.V. & Matar, O.K. 2020 Effect of surfactant on elongated bubbles in capillary tubes at high Reynolds number. *Phys. Rev. Fluids* **5** (9), 093605.

Carrier, O., Ergin, F.G., Li, H.Z., Watz, B.B. & Funfschilling, D. 2015 Time-resolved mixing and flow-field measurements during droplet formation in a flow-focusing junction. *J. Micromech. Microengng* **25** (8), 084014.

Chagot, L., Quilodrán-Casas, C., Kalli, M., Kovalchuk, N.M., Simmons, M.J.H., Matar, O.K., Arcucci, R. & Angeli, P. 2022 Surfactant-laden droplet size prediction in a flow-focusing microchannel: a data-driven approach. *Lab on a Chip* **22** (20), 3848–3859.

Chen, Y., Xu, J.-H. & Luo, G.-S. 2015 The dynamic adsorption of different surfactants on droplet formation in coaxial microfluidic devices. *Chem. Engng Sci.* **138**, 655–662.

Constante-Amores, C.R., Batchvarov, A., Kahouadji, L., Shin, S., Chergui, J., Juric, D. & Matar, O.K. 2021*a* Role of surfactant-induced Marangoni stresses in drop-interface coalescence. *J. Fluid Mech.* **925**, A15.

Constante-Amores, C.R., Kahouadji, L., Batchvarov, A., Shin, S., Chergui, J., Juric, D. & Matar, O.K. 2020 Dynamics of retracting surfactant-laden ligaments at intermediate Ohnesorge number. *Phys. Rev. Fluids* **5** (8), 084007.

Constante-Amores, C.R., Kahouadji, L., Batchvarov, A., Shin, S., Chergui, J., Juric, D. & Matar, O.K. 2021*b* Dynamics of a surfactant-laden bubble bursting through an interface. *J. Fluid Mech.* **911**, A57.

Craster, R.V., Matar, O.K. & Papageorgiou, D.T. 2002 Pinchoff and satellite formation in surfactant covered viscous threads. *Phys. Fluids* **14** (4), 1364–1376.

Dong, T., Weheliye, W. & Angeli, P. 2019 Laser induced fluorescence studies on the distribution of surfactants during drop/interface coalescence. *Phys. Fluids* **31**, 12106.

Dussaud, A.D., Matar, O.K. & Troian, S.M. 2005 Spreading characteristics of an insoluble surfactant film on a thin liquid layer: comparison between theory and experiment. *J. Fluid Mech.* **544**, 23–51.

Eggeling, C., Widengren, J., Rigler, R. & Seidel, C.A.M. 1998 Photobleaching of fluorescent dyes under conditions used for single-molecule detection: evidence of two-step photolysis. *Anal. Chem.* **70** (13), 2651–2659.

Filimonov, R., Wu, Z. & Sundén, B. 2021 Toward computationally effective modeling and simulation of droplet formation in microchannel junctions. *Chem. Engng Res. Des.* **166**, 135–147.

Garstecki, P., Stone, H.A. & Whitesides, G.M. 2005 Mechanism for flow-rate controlled breakup in confined geometries: a route to monodisperse emulsions. *Phys. Rev. Lett.* **94**, 164501.

Gassin, P.-M., Martin-Gassin, G., Meyer, D., Dufrêche, J.-F. & Diat, O. 2012 Kinetics of triton-x100 transfer across the water/dodecane interface: analysis of the interfacial tension variation. *J. Phys. Chem.* C **116** (24), 13152–13160.

Jin, F., Gupta, N.R. & Stebe, K.J. 2006 The detachment of a viscous drop in a viscous solution in the presence of a soluble surfactant. *Phys. Fluids* **18** (2), 022103.

Kahouadji, L., Nowak, E., Kovalchuk, N., Chergui, J., Juric, D., Shin, S., Simmons, M.J.H., Craster, R.V. & Matar, O.K. 2018 Simulation of immiscible liquid–liquid flows in complex microchannel geometries using a front-tracking scheme. *Microfluid Nanofluid* **22**, 126.

Kalli, M. & Angeli, P. 2022 Effect of surfactants on drop formation flow patterns in a flow-focusing microchannel. *Chem. Engng Sci.* **253**, 117517.

Kalli, M., Chagot, L. & Angeli, P. 2022 Comparison of surfactant mass transfer with drop formation times from dynamic interfacial tension measurements in microchannels. *J. Colloid Interface Sci.* **605**, 204–213.

Kamat, P.M., Wagoner, B.W., Thete, S.S. & Basaran, O.A. 2018 Role of marangoni stress during breakup of surfactant-covered liquid threads: reduced rates of thinning and microthread cascades. *Phys. Rev. Fluids* **3** (4), 043602.

KIRATZIS, I., KOVALCHUK, N.M., SIMMONS, M.J.H. & VIGOLO, D. 2022 Effect of surfactant addition and viscosity of the continuous phase on flow fields and kinetics of drop formation in a flow-focusing microfluidic device. *Chem. Engng Sci.* **248** (B), 117183.

KOVALCHUK, N.M., NOWAK, E. & SIMMONS, M.J.H. 2017 Kinetics of liquid bridges and formation of satellite droplets: difference between micellar and bi-layer forming solutions. *Colloids Surf.* A **521**, 193–203.

KOVALCHUK, N.M., ROUMPEA, E., NOWAK, E., CHINAUD, M., ANGELI, P. & SIMMONS, M.J.H. 2018 Effect of surfactant on emulsification in microchannels. *Chem. Engng Sci.* **176**, 139–152.

KOVALCHUK, N.M. & SIMMONS, M.J.H. 2021 Effect of surfactant dynamics on flow patterns inside drops moving in rectangular microfluidic channels. *Colloids Interfaces* **5** (3), 40.

LAN, W., LI, S., WANG, Y. & LUO, G. 2014 CFD simulation of droplet formation in microchannels by a modified level set method. *Ind. Engng Chem. Res.* **53** (12), 4913–4921.

LAWRENCE, M.J. & REES, G.D. 2000 Microemulsion-based media as novel drug delivery systems. *Adv. Drug Deliv. Rev.* **45** (1), 89–121.

LEONG, C.M., GAI, Y. & TANG, S.K.Y. 2018 Internal flow inside droplets within a concentrated emulsion during droplet rearrangement. *Phys. Fluids* **30** (3), 032002.

LI, D., ZHOU, L., YU, Q., PU, X., SUN, Y., ZHOU, Q. & ZHANG, Y. 2022 Optical fiber optofluidic laser based on surfactant solubilization of rhodamine b gain in an aqueous solution. *Opt. Express* **30** (13), 23295–23304.

LI, X.-B., LI, F.-C., YANG, J.-C., KINOSHITA, H., OISHI, M. & OSHIMA, M. 2012 Study on the mechanism of droplet formation in t-junction microchannel. *Chem. Engng Sci.* **69** (1), 340–351.

MARTIN, J.D. & HUDSON, S.D. 2009 Mass transfer and interfacial properties in two-phase microchannel flows. *New J. Phys.* **11** (11), 115005.

MIESSNER, U., HELMERS, T., LINDKEN, R. & WESTERWEEL, J. 2020 μpiv measurement of the 3d velocity distribution of Taylor droplets moving in a square horizontal channel. *Exp. Fluids* **61**, 125.

MURADOGLU, M. & TRYGGVASON, G. 2014 Simulations of soluble surfactants in 3d multiphase flow. *J. Comput. Phys.* **274**, 737–757.

NGO, I.-L., DANG, T.-D., BYON, C. & JOO, S.W. 2015 A numerical study on the dynamics of droplet formation in a microfluidic double t-junction. *Biomicrofluidics* **9** (2), 024107.

PARK, D., KIM, H. & KIM, J.W. 2021 Microfluidic production of monodisperse emulsions for cosmetics. *Biomicrofluidics* **15** (5), 051302.

PIRBODAGHI, T., VIGOLO, D., AKBARI, S. & DEMELLO, A. 2015 Investigating the fluid dynamics of rapid processes within microfluidic devices using bright-field microscopy. *Lab on a Chip* **15** (9), 2140–2144.

RIAUD, A., ZHANG, H., WANG, X., WANG, K. & LUO, G. 2018 Numerical study of surfactant dynamics during emulsification in a t-junction microchannel. *Langmuir* **34** (17), 4980–4990.

ROUMPEA, E., KOVALCHUK, N.M., CHINAUD, M., NOWAK, E., SIMMONS, M.J.H. & ANGELI, P. 2019 Experimental studies on droplet formation in a flow-focusing microchannel in the presence of surfactants. *Chem. Engng Sci.* **195**, 507–518.

SHIN, S., ABDEL-KHALIK, S.I., DARU, V. & JURIC, D. 2005 Accurate representation of surface tension using the level contour reconstruction method. *J. Comput. Phys.* **203** (2), 493–516.

SHIN, S., CHERGUI, J. & JURIC, D. 2017 A solver for massively parallel direct numerical simulation of three-dimensional multiphase flows. *J. Mech. Sci. Technol.* **31** (4), 1739–1751.

SHIN, S., CHERGUI, J., JURIC, D., KAHOUADJI, L., MATAR, O.K. & CRASTER, R.V. 2018 A hybrid interface tracking – level set technique for multiphase flow with soluble surfactant. *J. Comput. Phys.* **359**, 409–435.

SHIN, S. & JURIC, D. 2002 Modeling three-dimensional multiphase flow using a level contour reconstruction method for front tracking without connectivity. *J. Comput. Phys.* **180** (2), 427–470.

SOH, G.Y., YEOH, G.H. & TIMCHENKO, V. 2016 Numerical investigation on the velocity fields during droplet formation in a microfluidic t-junction. *Chem. Engng Sci.* **139**, 99–108.

TEIPEL, U. & AKSEL, N. 2001 Adsorption behavior of nonionic surfactants studied by drop volume technique. *Chem. Engng Technol.* **24** (4), 393–400.

VAN DER GRAAF, S., NISISAKO, T., SCHROËN, C.G.P.H., VAN DER SMAN, R.G.M. & BOOM, R.M. 2006 Lattice Boltzmann simulations of droplet formation in a t-shaped microchannel. *Langmuir* **22** (9), 4144–4152.

WANG, K., LU, Y.C., XU, J.H & LUO, G.S. 2009 Determination of dynamic interfacial tension and its effect on droplet formation in the t-shaped microdispersion process. *Langmuir* **25** (4), 2153–2158.

WEE, H., WAGONER, B.W., GARG, V., KAMAT, P.M. & BASARAN, O.A. 2021 Pinch-off of a surfactant-covered jet. *J. Fluid Mech.* **908**, A38.

WILKE, C.R. & CHANG, P. 1955 Correlation of diffusion coefficients in dilute solutions. *AIChE J.* **1** (2), 264–270.

XU, J.H., DONG, P.F., ZHAO, H., TOSTADO, C.P. & LUO, G.S. 2012 The dynamic effects of surfactants on droplet formation in coaxial microfluidic devices. *Langmuir* **28** (25), 9250–9258.

XU, J.H., LUO, G.S., LI, S.W. & CHEN, G.G. 2006 Shear force induced monodisperse droplet formation in a microfluidic device by controlling wetting properties. *Lab on a Chip* **6**, 131–136.

YANG, L., KAPUR, N., WANG, Y., FIESSER, F., BIERBRAUER, F., WILSON, M.C.T., SABEY, T. & BAIN, C.D. 2018 Drop-on-demand satellite-free drop formation for precision fluid delivery. *Chem. Engng Sci.* **186**, 102–115.

ZHAO, S., RIAUD, A., LUO, G., JIN, Y. & CHENG, Y. 2015 Simulation of liquid mixing inside micro-droplets by a lattice Boltzmann method. *Chem. Engng Sci.* **131**, 118–128.